Combined Modalities of Compton Scattering Tomography

Gaël Rigaud, Rémi Régnier, Maï K. Nguyen, and Habib Zaidi, *Senior Member, IEEE*

***Abstract*—The requirement to scope and analyze hidden parts of the human body and the limitations of current imaging technologies is motivating the development of novel approaches. In clinical PET/CT systems, the attenuation and activity maps of the studied body region are recovered from measurements. However, the modeling of Compton scattering enables to obtain the attenuation map through the electron density directly from transmission data, thus obviating the need of a CT scan. In this context, a bimodality imaging approach (gamma-ray transmission/emission imaging) using scattered radiation referred to as *Compton scattering tomography* (CST) is presented. This concept is modeled by two generalized Radon transforms and proposes to reconstruct the electron density, the attenuation map, and the activity concentration of the studied body region. Simulation results demonstrate the feasibility and viability of this novel imaging concept. The present approach could be an interesting alternative to current tomographic imaging techniques.**

***Index Terms*—Attenuation correction, bimodal imaging, Compton scattering tomography (CST), emission imaging, image reconstruction, Radon transform, transmission imaging.**

I. Introduction

THE requirement for fast and realiable diagnostics or therapy planning in modern healthcare systems has led to a wealthy development of hybrid imaging technologies. While traditional imaging techniques such as X-ray computed tomography (CT) and magnetic resonance imaging (MRI) provide information on a patient's anatomy or on the location and extent of the disease, positron emission tomography (PET) and single-photon emission computed tomography (SPECT) are able to detect biomolecular changes (even prior to anatomic change) and the biochemical status or the physiological function of a human organ. The idea of combining imaging techniques has become a very useful clinical tool. The introduction of combined PET/CT scanners revolutionized clinical practice and received widespread clinical acceptance [1]. PET/MRI hybrid systems combining PET and MR devices to obtain anatomical and molecular information simultaneously appeared later [2].

Nowadays, we observe that three major medical imaging modalities (i.e., CT, SPECT, and PET) make use only of primary radiation whereas scattered radiation is considered as noise and then is routinely eliminated, or at least compensated for [3]. Thus, the idea is to explore whether a bimodal imaging system can be built based exclusively on the exploitation of scattered radiation. Imaging with scattered radiation has a long story since it has been initiated during the 1950's, at a time when research on SPECT, PET, and CT imaging had just started. The central idea of scattered radiation imaging is based on Compton scattering effect. Different approaches were suggested by various groups, and the concept of Compton scattering tomography (CST) has emerged as a key idea for building a CST scanner, which could be as efficient as scanners using primary radiation [4]–[7]. The concept was further promoted by pioneering work performed by Norton in 1994 [8]. At the beginning of the twenty-first century, a further advance was made in the use of scattered radiation for imaging, to be feasible for emission imaging. For a radiating (or made radiating) object, a SPECT gamma camera can be set to register, without having to rotate around this object, a set of images at different scattered energies. To use an optical analogy, it is as if the gamma camera records images at different wavelengths or using different color filters. The crux of the matter is that one can show that from this data set, a three-dimensional object reconstruction is possible. Moreover, a two-dimensional version of this scattered radiation has been shown to be feasible in the last few years, referred to as V-line emission imaging (VEI) [9], [10]. Thus, it is tempting (and logical) to combine Compton scattering tomography with V-line emission imaging as the first bimodal scatter radiation imaging, which is the topic of this work.

In this paper, we propose a new concept of bimodality imaging based on Compton scattering tomography modalities similar to the PET/CT system in the sense that it combines transmission and emission modalities. In our novel imaging system, we consider two CST modalities. The first one works in transmission; the modeling of its image formation is based on a circular-arc Radon transform (CART). The second one works in emission; it is based on a compounded V-line Radon transform (CVRT).

Image quality in functional imaging is still a major issue in the medical research domain [11], [12]. In this context, the proposed system aims to increase image quality in emission tomography through the use of the single scattered radiation (which represents 80% of the emitted radiation) and suited correction algo-

Manuscript received September 25, 2012; revised January 09, 2013 and February 11, 2013; accepted February 25, 2013. Date of publication April 30, 2013; date of current version June 12, 2013. The work of R. Régnier is supported by DGA.

G. Rigaud, R. Régnier, and M. K. Nguyen are with the ETIS Laboratory—ENSEA/Univ. Cergy-Pontoise/CNRS, 95000 Cergy-Pontoise, France (e-mail: gael.rigaud@gmail.com; regnierremi@yahoo.fr; mai.nguyen-verger@u-cergy.fr).

H. Zaidi is with the Geneva University Hospital, Division of Nuclear Medicine and Molecular Imaging, CH-1211 Geneva 4, Switzerland; Geneva University, Geneva Neuroscience Center, CH-1205 Geneva, Switzerland; and the Department of Nuclear Medicine and Molecular Imaging, University Medical Center Groningen, University of Groningen, 9700 RB Groningen, The Netherlands (e-mail: habib.zaidi@hcuge.ch).

Color versions of one or more of the figures in this paper are available online at http://ieeexplore.ieee.org.

Digital Object Identifier 10.1109/TNS.2013.2252022

rithm. Another interest of this combination is that both modalities allow a two-dimensional image reconstruction from any scattered radiation collected by a one-dimensional collimated nonmoving camera. This involves a new concept of detector with high-energy resolution able to collect the scattered radiation.

The physics of the Compton effect allows the reconstruction of the electron density, which is linked to the attenuation map and thus contributes to the modeling of emission CST. This shows the complementarity of the two CST modalities.

The electron density n_e of a studied object is nonconstant, and this has a huge impact on emission CST to such an extent that it is impossible to reconstruct a coherent activity map. Fortunately, the reconstruction of the electron density map is provided by the transmission CST; therefore, we use it as prior information for the correction of the second CST reconstruction. Moreover, one creates the rough attenuation map linked to the electron density and uses it in an attenuation correction iterative algorithm. The main idea of this algorithm is the creation of an attenuation map to correct the electron density, which will create a new attenuation map and iterate this algorithm until the convergence of the algorithm is reached. Also, we use the final attenuation map to correct the map of the emission CST.

The paper is organized as follows. Section II deals with the concept of our Compton scattering tomography bimodality through the transmission one as proposed by Norton in 1994 [8] and the emission one as proposed by Nguyen and Truong in 2011 [10]. Image formation is also introduced. In Section III, we present the inversion of the original data, their attenuation, and electron density correction through a suited correction algorithm, in which we take into account physical phenomena such as attenuation factor. Finally, in Section IV, we present new numerical results of the emerging CST system on a slice of the Zubal phantom [13].

II. Theory

In this section, we present the measurement model of our combined system (Fig. 1). In this concept, a patient is submitted to two examinations in order to recover three information maps: the electron density, the attenuation map, and the activity (tracer). We will see in the next section how we deduce the attenuation map from the electron density through the proposed algorithm. These examinations are modeled by two modalities of CST: CST_1 and CST_2. First, we introduce the anatomic examination proposed by Norton [8] and modeled by a circular-arc Radon transform. In this paper, we try to take into account physical factors. This is why our modeling is more complex than the one shown by Norton. Then, we present the functional examination that was proposed by Truong and Nguyen [10] and that is modeled by a compounded V-line Radon transform.

A. Compton Scattering Tomography Modality Based on Circular-Arc Radon Transform

The working principle of Norton's modality [8] is given by Fig. 2. In an idealized context (without attenuation and radiation spreading effects), in order to convey the basic idea, a point-like source **S** emits primary radiation towards an object, of which **M**

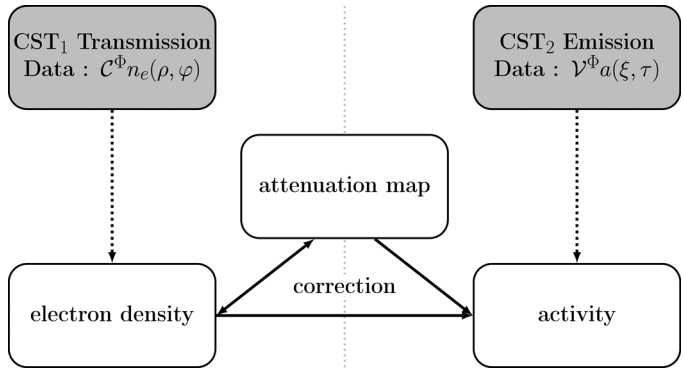

Fig. 1. Concept of a novel bimodal system.

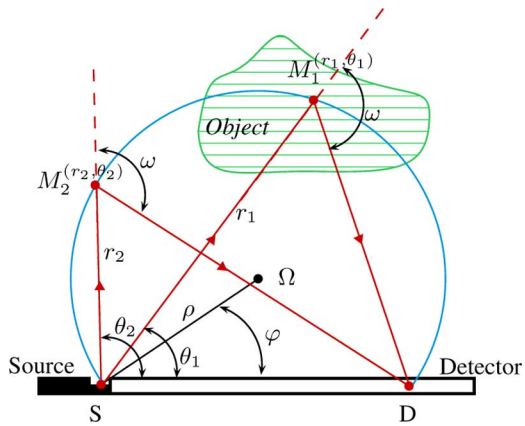

Fig. 2. Principle of Norton's modality of Compton scattering tomography.

is a scattering site (running point). Also a point-like detector **D** moves along an *Ox*-axis and collects, at given energy E_ω, scattered radiation from the object. The physics of Compton scattering requires that the registered radiation flux density $g(\mathbf{D})$ at site **D** is due to the scattering contribution of all scattering sites **M** lying on an arc of circle from **S** to **D** subtending an angle $(\pi-\omega)$, where ω is the scattering angle corresponding to the outgoing energy E_ω.

In the absence of attenuation, Norton wrote down the expression of the received radiation flux density at **D** in $\mathbb{R}^2$. As we want to take into account the attenuation factor in the modeling of the CART, we have to rewrite the projections $g(\mathbf{D})$ as

$$\mathcal{C}^{\Phi} n_e(\rho,\varphi) = \int_0^{\pi}\int_0^{\infty} n_e(r,\theta)\, \mathcal{K}_{\mathcal{C}}(r,\theta|\rho,\varphi)\, w_{att}(\rho,\varphi,r,\theta) r\, dr\, d\theta \quad (1)$$

with

$$\mathcal{K}_{\mathcal{C}}(r,\theta|\rho,\varphi) = \frac{r^2\, s(\theta)\, \sigma^c(\omega)}{4\pi\, (2\rho)^3\, \sin^2\theta}\, \delta\left[r - 2\rho\cos(\theta-\varphi)\right]$$

where $s(\theta)$ expresses any angular dependence of the gamma-ray source distribution, and $\sigma^c(\omega)$ is the Klein–Nishina differential cross section and

$$w_{att}(\rho,\varphi,r,\theta) = \exp\left(-\int_0^{r} \mu_0(t\cos\theta, t\sin\theta)dt - \int_0^{r_1} \mu_\omega(r\cos\theta + t\cos(\omega-\theta), r\sin\theta + t\sin(\omega-\theta))dt\right),$$

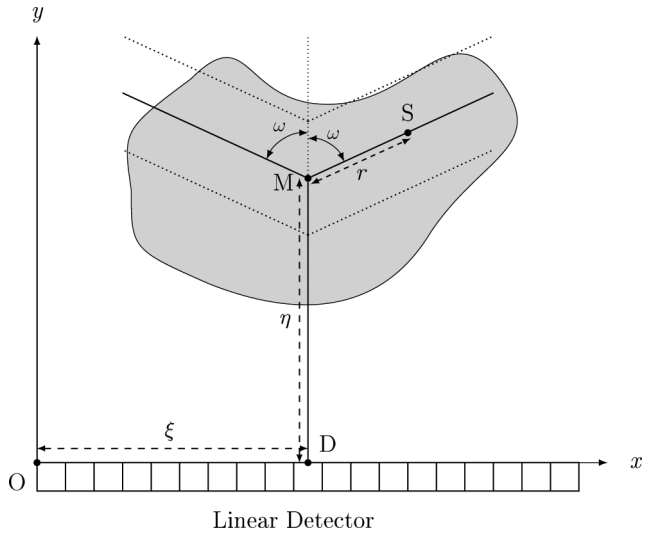

Fig. 3. Principle of compounded $\mathcal{V}$-line Radon transform and parameters setup.

with $r_1 = r\sin\theta/\sin(\theta-\omega)$. Mathematically, $\mathcal{C}^{\Phi}n_e(\rho,\varphi)$ is essentially the Radon transform of the object electron density $n_e(r,\theta)$ on arcs of circle passing through a fixed point $\mathbf{S}$ of equation $r = 2\rho\cos(\theta-\varphi)$.

The factor w_{att} cannot be separated in a product $w_1(r,\theta)\cdot w_2(\rho,\varphi)$; this is why the Cormack inversion procedure cannot be applied [14], [15]. For the moment, we do not know how to invert analytically the attenuated CART. For this, we propose an attenuation correction algorithm in order to compensate the attenuation factor.

B. Compton Scattering Tomography Modality by Emission Based On Compounded $\mathcal{V}$-Line Radon Transform

The working principle of the CVRT [10] is given by Fig. 3. In order to convey the basic idea, a 2D-object containing a nonuniform radioactivity source distribution emits primary radiation. Also, a collimated linear static detector collects, at given energy E_ω, scattered radiation from the object with a direction parallel to that of the collimator holes. The physics of Compton scattering requires that the registered radiation flux density $g(\mathbf{D})$ at site $\mathbf{D}$ is due to the sum of the contribution of all emitting object point sources located on two half-lines starting at a site $\mathbf{M}$ and making an angle ω with the collimator axis direction, for all possible $\mathbf{M}$ along the axis of the collimator at $\mathbf{D}$.

Let $a(x,y)$ be an activity density function. We consider the physical phenomena, as follows:

1) the photon flux is submitted to an attenuation map μ_0 between each internal source to the scattering points;
2) the probability of diffusion being proportional in the electronic density, it is necessary to take care of the nonhomogeneous $n_e(\mathbf{M})$;
3) the spreading photon flux propagates up to the detector with a new scattering energy (see Compton formula) and so is attenuated by μ_ω.

With all these considerations, the measured photon flux density at $\mathbf{D}$ under a scattering angle ω can be written as

$$\mathcal{V}^{\Phi}a(\xi,\tau) = P(\tau)\int_{\mathbb{R}^2} dxdy\,\mathcal{K}_{\mathcal{V}}(x,y|\xi,\tau)\; w_v^{\phi}(\xi,\eta,r)a(x,y), \tag{2}$$

with $\tau = \tan(\omega)$ and

$$\mathcal{K}_{\mathcal{V}}(x,y|\xi,\tau) = \frac{1}{4\pi^2|x-\xi|}\frac{Y(y-|x-\xi|\tau)}{y-|x-\xi|\tau},$$

$$w_v^{\phi}(\xi,\eta) = n_e(\xi,\eta)\exp\left(-\int_0^{\eta}\mu_\omega(\xi,\eta')d\eta'\right)$$

$$\times e^{-\int_0^r \mu_0(\xi+r'\sin\omega,\eta+r'\cos\omega)dr' - \int_0^r \mu_0(\xi-r'\sin\omega,\eta+r'\cos\omega)dr'}.$$

Equation (2) stands for image formation, but this form does not permit the inversion procedure without correcting the additional physical factors w_v^{ϕ} through a correction algorithm. Without this factor, we can use the inversion proposed in [10]. Nevertheless, to avoid singularities, we consider that the object of interest is placed at a minimal distance from the detector. The global inversion algorithm will be present in the next section.

III. Algorithm Description

A. Suited Attenuation/Electron Density Correction Algorithm for Both Radon Transforms

Numerous methods for correcting the attenuation factor were proposed: for example, the generalized Chang correction (GCC), which corrects the reconstructed function or the iterative pre correction (IPC), which corrects data; see [16]. Nevertheless, these algorithms need the attenuation map. Here, we cannot have this information since we want to recover the attenuation map from the electron density. To avoid such assumption, we propose an alternative IPC algorithm in which the attenuation map is obtained iteratively from the electron density, making the assumption that we know the kind of the medium and so the corresponding total cross section. Thus, an approximated attenuation map is deduced from the approximated electron density and is used to correct the data. We iterate until convergence of the algorithm is reached.

In this part, we denote by T the operator $\mathcal{C}$ (respectively, $\mathcal{V}$) and by $(\mathcal{X},\mathcal{Y})$, the measurable space $(\mathbb{R}^+\times[0,\pi],\mathbb{R}^+\times[0,2\pi[)$ (respectively, $(\mathbb{R}^+\times\mathbb{R}^+,\mathbb{R}^+\times[0,\pi])$).

Assuming that the studied image f can be reconstructed from its measurement Tf, the following recurrence relation converges towards f:

$$f^{n+1} = f^n + T^{-1}\circ T^{\Phi}(f-f^n) \qquad \text{with} \qquad f^0 = 0. \tag{3}$$

See the Appendix for the proof of the convergence of (3). This algorithm requires an analytical inversion of the mathematical modeling of our modalities. We give these inversion formulas below.

B. Estimation of the Attenuation Map

In the context of a medical application, we can use prior knowledge about the studied slice. Thus, we assume in our case that the studied body (in term of attenuation factor) is composed of known substances. Then, we can deduce from the electron density an approximative attenuation map. The idea is then to deduce at each iteration the attenuation map from the current reconstructed electron density using a k-means clustering. This has the advantage to improve the quality of reconstruction of

the electron density and to reconstruct an approximative attenuation map which is necessary to correct the activity in the emission CST modality.

C. CART: Inversion Formula via Circular Harmonic Decomposition

Norton worked out an inverse formula [8] which can be interpreted as a back-projection procedure on arcs of circle and not on straight lines as in the case of classical Radon transform. Norton has produced also numerical simulations to validate his modality first without attenuation effects. In a next step, he has also developed related numerical algorithms in which he took approximately into account the attenuation in matter for a point object [8]. His results have appeared as quite convincing.

In our study, we will use a different reconstruction. Based on Cormack's works [14], [15], it produces a consistent reconstructed image in the circular harmonic components domain. To invert this transform, we cannot take into account the attenuation factor. We start from (1). Let

$$\begin{cases} \mathcal{C}f(p,\varphi) = \mathcal{C}^{\Phi} n_e(\frac{p}{2},\varphi)\ \frac{p^4}{P\left(\varphi+\frac{\pi}{2}\right)} \\ f(r,\theta) = n_e(r,\theta)\ \frac{bs(\theta)r}{8\pi \sin^2\theta}. \end{cases} \tag{4}$$

Substituting (4) in (1), we obtain

$$\mathcal{C}f(p,\varphi) = \int_0^{\pi} d\theta \int_0^{+\infty} dr\ p\ f(r,\theta)\ \delta\left\{r - p\cos(\theta-\varphi)\right\}.$$

This equation gives the integral of a function $f(r,\theta)$ on a class of circles having a fixed common point of equation $r = p\cos(\theta-\varphi)$ and defined by the integral kernel support in (r,θ)-space. This equation belongs to the β-curve $(\beta = 1)$ family of [14] and so is suitable for circular harmonic decomposition. This is why the inverse transform can be worked out using the Fourier angular components of f and $\mathcal{C}f$.

$$f_l(r) = \frac{1}{\pi r}\int_0^r \frac{e^{-|l|\cosh^{-1}(r/p)}}{\sqrt{(\frac{r}{p})^2-1}}\ (\mathcal{C}f_l)'(p)dp - \frac{1}{\pi r}\int_r^{+\infty} U_{|l|-1}\left(\frac{r}{p}\right)\ (\mathcal{C}f_l)'(p)dp \tag{5}$$

where $U_{l-1}(\cos x) = \sin lx/\sin x$ is the Tchebychev polynomial of second kind. Finally, $f(r,\theta)$ is reconstructed through its Fourier expansion with the circular harmonic components $f_l(r)$. Thus, by a change of functions (4), we can study the modeling of the Norton's CST as the inversion of the transform $\mathcal{C}$ in the (p,φ)-space. For more details about the numerical implementation, see [17].

D. CVRT: Inversion Formula

The proposed algorithm needs the analytical inversion of the modelling of the CST_2 without attenuation then the Klein–Nishina scattering probability in Compton effect is discarded. Let us define

$$h(x,y) = \int_0^{+\infty} \frac{d\eta}{2\pi\eta} a(x,\eta+y).$$

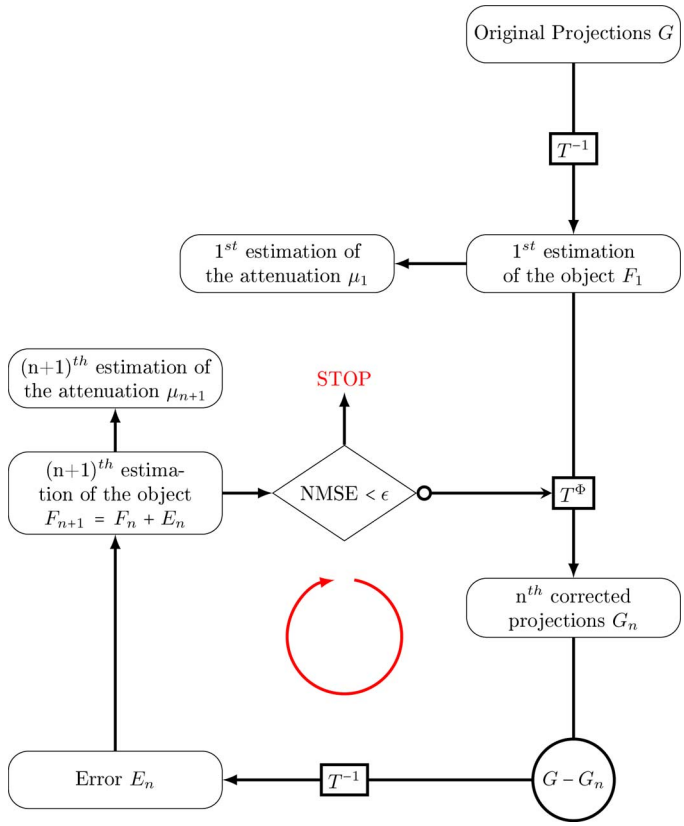

Fig. 4. Proposed attenuation/electron density correction algorithm for both modalities. The parameter ϵ is an object-dependent threshold.

The inversion of the CVRT has been established in [10], and the inversion formula is

$$a(x,y) = \int_{-\infty}^{+\infty}\int_{-\infty}^{+\infty} \frac{e^{2i\pi q(y-z)}h(x,z)}{\gamma + i\frac{\pi}{2}sgn(q) - \ln(2\pi|q|)}dzdq \tag{6}$$

with

$$h(x,z) = \frac{z}{\pi}\int_0^{\pi/2} p.v.\left(\int_{\mathbb{R}} \frac{\mathcal{V}\tilde{a}(u,\omega)}{u - x\cos\omega \pm z\sin\omega}du\right)\frac{d\omega}{\cos\omega} + \frac{z}{\pi}\int_0^{\infty} p.v.\left(\int_{\mathbb{R}} \frac{\mathcal{V}a(\xi,-\tau)}{\xi - x \pm z\tau}d\xi\right)d\tau,$$

putting $\omega = \arctan\tau$, $u = \xi\cos\omega$ and $\mathcal{V}\tilde{a}(u,\omega) = \mathcal{V}a(\xi,\tau)$. As this expression can be rewritten as a simple backprojection over corresponding broken lines convolved with a filter, it does not need a computational regularization.

E. Simulation Studies

We propose to test our approach on a slice of the Zubal phantom [13], which represents the thorax Fig. 5. The aim of this experiment is to detect a cardiac biodistribution. We use the Hounsfield scale to deduce from water the electron density and the attenuation coefficient of a given matter at a given energy. Moreover, we try to detect tumorous lesions by introducing a tracer into the body. The activity is equal to 13 MBq, and the value HU (Hounsfield unit) is equal to 50.

Fig. 5. Slice of Zubal phantom.

We just consider seven kinds of substances: air, water, lung, bone (for organ categories 5 and 11), muscle (for organ categories 6 and 8), and blood and tissue (for organ categories 2 and 9).

The scattering medium is discretized with 128×128 pixels. We consider the number of detector positions $(N_x,\ N_\varphi)$ and the number of energy levels N_ω. In order to have a "well-conditioned" problem, the number of projections $(N_x \times N_\omega,\ N_\varphi \times N_\omega)$ must be larger than the number of image pixels (128×128). As the measurement space is very large (because the system does not work with rotation around the body), we have to take a very large number of projections; this is why we choose $N_x = N_\varphi = N_\omega = 512$. This leads to the choice of scattering angular sampling step $\Delta\omega = 0.53^\circ$, which means, by differentiating the Compton energy formula and averaging over the scattering angle, an energy resolution of $\Delta E = 1.5$ eV for the most commonly used radionucleide (^{99m}Tc) having an energy $E_0 = 140$ keV (or $\Delta E = 10$ eV for $E_0 = 511$ keV). If $N_\omega < 512$, the required energy resolution may be larger, but the resulting image resolution is reduced.

It should be noted that no desampling is applied in the following numerical results. The high order of the resolution $(N_x,\ N_\varphi,\ N_\omega)$ is due to noncompact data space. As such, we had to increase the sampling to guarantee a solution for the studied inverse problem.

Fig. 6(a) shows the computation of the forward modeling of the measurement obtained for the studied medical phantom (Fig. 5). These data follows the shape of the point spread function given by the integral kernel $\mathcal{K}_\mathcal{C}(r, \theta|\rho, \varphi)$.

We present now the results of numerical data set simulation [see Fig. 6(b)] for our experiment protocol. We note the characteristic shape of the V-lines Radon transform, i.e., a form of "V" slightly curvilinear for high values of scattering angle with an intensity leveling off when the angle increases which is coherent with the PSF function.

Before applying the correction algorithm, we give the reconstructions of the electron density [Fig. 6(c)] and of the activity [Fig. 6(d)] of the thorax phantom obtained without correction.

Since photon emission process follows Poisson's law, this phenomenon is one of the main cause of degradation of the quality of image reconstruction in Compton scattering

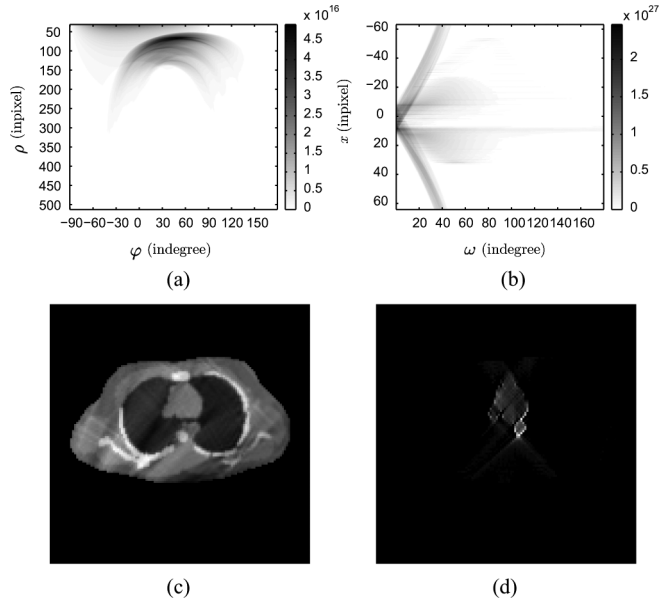

Fig. 6. (a) CART and (b) CVRT of the phantom shown in Fig. 5. Reconstruction of the (c) electron density and (d) activity distribution using (5) and (6), respectively, without noise and correction.

tomography. Thus, the projections become in both cases $\tilde{g}(\mathbf{t}) \sim \mathcal{P}(Tf(\mathbf{t}))$, where $\mathcal{P}$ stands for the Poisson law.

We define a signal-to-noise ratio (SNR) by

$$\mathrm{SNR} = 10 \log \left(\frac{\int_{\mathbf{t}\in\mathcal{T}} Tf(\mathbf{t})^2 d\mathbf{t}}{\int_{\mathbf{t}\in\mathcal{T}} |\tilde{g}(\mathbf{t}) - Tf(\mathbf{t})|^2 d\mathbf{t}} \right).$$

Here, we study the robustness of our algorithms, taking into account this phenomenon. The denoising is performed for the results presented below using the suited Poisson noise algorithm shown in [18].

IV. Results

We follow the scheme presented in Fig. 1. Therefore, we first reconstruct the electron density, then the attenuation map is deduced from the first approximation of n_e, and we iterate the proposed correction algorithm (3) to obtain final n_e and attenuation map. Once the first algorithm performed (representing the CST_1), we reconstruct the activity, and we correct it by using the proposed correction algorithm, the attenuation map, and n_e.

To assess the quality of the reconstructions, we define the normalized mean-square error (NMSE) as

$$\mathrm{NMSE} = \frac{1}{N^2} \frac{\sum_{(i,j)\in[1,N]^2} |\mathcal{I}_r(i,j) - \mathcal{I}_o(i,j)|^2}{\max_{(i,j)\in[1,N]^2} \{\mathcal{I}_o(i,j)\}^2}$$

where $\mathcal{I}_r$ is the reconstructed image, and $\mathcal{I}_o$ the original image. This metric represents a good criterion for convergence of our iterative algorithm. Thus, we stop the iterations when the difference of NMSE between two iterations is smaller than 0.1%.

For our simulations, we considered noise with an SNR of 20–30 dB. Indeed, to keep the inversion problem feasible multiple scattering was ignored. This phenomenon will act as additional noise in our simulations. The choice of 20 or 30 dB

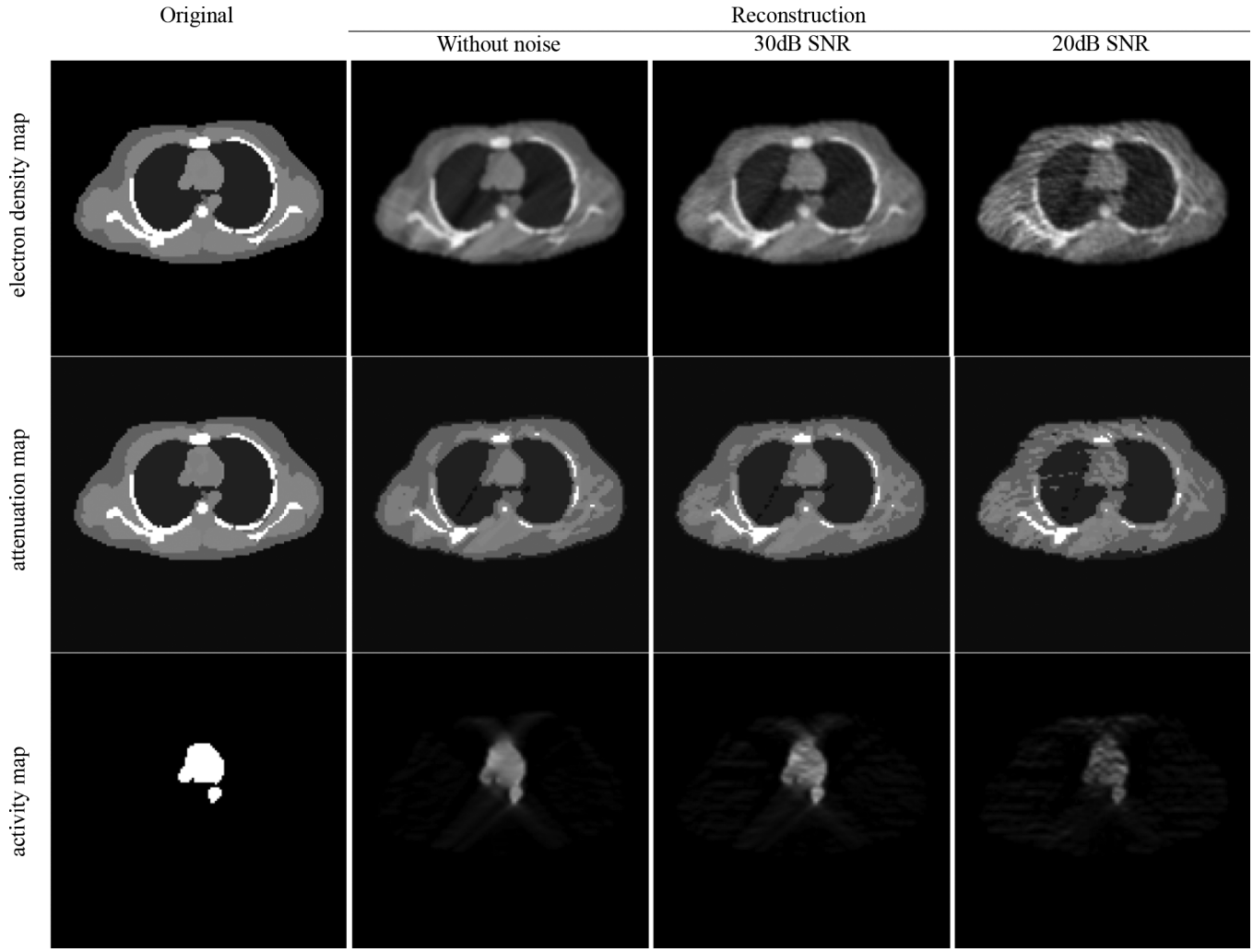

Fig. 7. Different reconstructions of the electron density map, attenuation map for different SNR. Reconstructions are obtained using the proposed correction algorithm and a Poisson noise process. We start these algorithms with data in Fig. 6(a) and (b).

is realistic in tomographic imaging applications, but further investigations should focus on evaluating the impact of various magnitudes of noise.

Fig. 7 shows the reconstructions of the thorax phantom shown in Fig. 5. We use the measurements shown in Fig. 6(a) for CART and in Fig. 6(b) for CVRT but with different SNRs. Reconstructions in Fig. 7 show a good quality for the electron density and the activity. Fig. 8 gives the NMSE in terms of iterations. We can see the interest of our method in terms of quality of reconstruction but in terms of magnitude as well. In the case of the CVRT, the initial error is very important (because of the electron density that we don't take into account). Nevertheless, the correction algorithm permits to decrease drastically the NMSE, even for a noise of 20 dB. In the case of the CART, the initial error is less important (only the attenuation is not taken into account), and the algorithm permits to obtain good NMSE.

The proposed algorithm makes use of the original algorithm to invert the projection data without considering attenuation. Both algorithms have been compared on the same datasets to demonstrate the benefit of the novel algorithm (see NMSE curves). Mathematically, the derivation presented in the Appendix shows that the proposed algorithm applied on attenuated data tends towards the reconstruction obtained using the original algorithm on unattenuated data. Thus, we can compare them with those obtained without attenuation [see Fig. 9(c) and (d)]. One can notice the good agreement between the results, which proves numerically the good convergence of our algorithm.

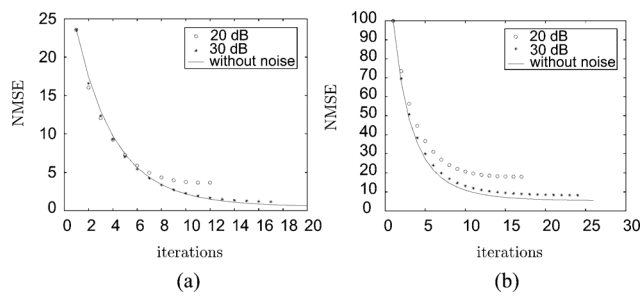

Fig. 8. NMSE in terms of iterations for the correction (a) of the electron density and (b) of the activity map for different SNR.

In this work, only single scattering was considered, assuming that higher order scattering occurs with much smaller probability going as the power of the Klein–Nishina probability [19]. As such, the effects of higher order scattering may be assimi-

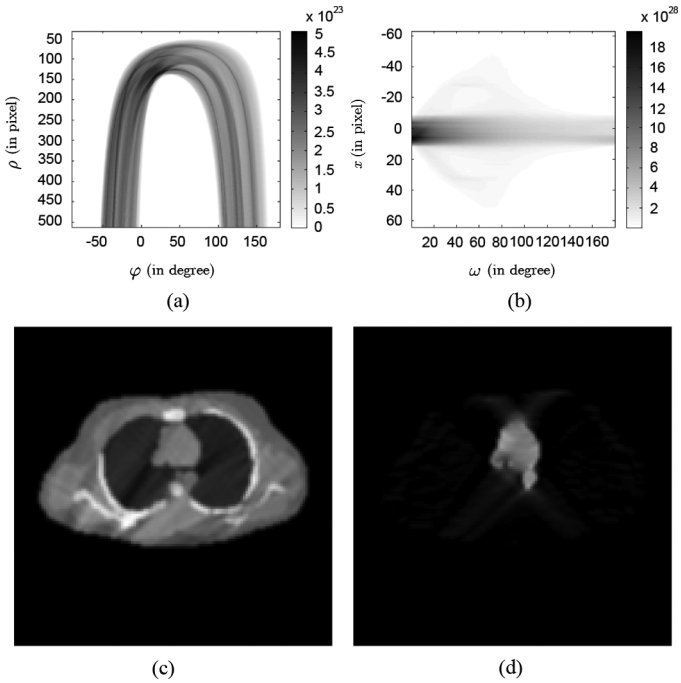

Fig. 9. (a) CART and (b) CVRT of the phantom shown in Fig. 5 without attenuation. Reconstruction of the (c) electron density and (d) activity distribution with the analytical inversion formulae.

lated to noise fluctuations. As mentioned earlier, the spatial and energy resolutions required for implementation of this approach are not yet achievable with current imaging devices. However, it is anticipated that future advances in detector technology will enable the design and fabrication of systems having the required performance characteristics.

These experiments prove the theoretical feasibility and the interest of this approach in medical applications.

V. Conclusion

The new CST approach proposes an alternative to current tomographic imaging techniques by keeping almost the same quality of reconstructions. In this paper, we have shown that a transmission Compton tomography modality can be combined with emission Compton tomography to form a new bimodal imaging system based on scattered radiation. The first CST modality characterizes the studied material directly by its electron density (scattering sites) and permits reconstructing an approximative attenuation map. In addition, the latter enables to reconstruct the activity map of the studied region of the human body. As such, the reconstruction of the electron density and of the attenuation map enables us to obtain a reasonable reconstruction of the activity through a suited correction algorithm. The latter is shown to be efficient for the correction of nonlinear factors in the context of generalized Radon transforms, and as such, is particularly suited for the targeted application.

Both imaging modalities seem to be feasible and complementary, as demonstrated by simulation studies, and appear as an alternative to current tomographic imaging techniques by keeping a good quality of reconstructions without rotational motion around the studied object.

Appendix A
Glossary

Acronyms		
CST		Compton scattering tomography
CST_1		CST by transmission
CST_2		CST by emission
CART		Circular-arc Radon transform
CVRT		Compounded V-line Radon transform
NMSE		Normalized mean-squared error
SNR		Signal-to-noise ratio
HU		Hounsfield unit
$p.v.$		Cauchy principal value
Functions		
$\delta(.)$	$\in \mathbb{R}$	1D Dirac function
$sgn(.)$	$\in \mathbb{R}$	sign function
E_ω	$\in \mathbb{R}^+$	photon energy of a Compton scattering of angle ω
$\phi(M_1 \to M_2)$	$\in \mathbb{R}^+$	photon flux density from M_1 to M_2
$n_e(r,\theta)$	$\in \mathbb{R}^+$	object electron density in polar coordinates
$\mu_\omega(x,y)$	$\in \mathbb{R}^+$	object attenuation map in cartesian coordinates at energy E_ω
$a(x,y)$	$\in \mathbb{R}^+$	source activity in cartesian coordinates
$\mathcal{C}^\Phi n_e(\rho,\varphi)$	$\in \mathbb{R}^+$	measurement obtained by CST_1
$\mathcal{V}^\Phi a(\xi,\tau)$	$\in \mathbb{R}^+$	measurement obtained by CST_2
$\mathcal{C}f(p,\varphi)$	$\in \mathbb{R}^+$	CART of a function $f(r,\theta)$
$\mathcal{V}f(\xi,\tau)$	$\in \mathbb{R}^+$	CVRT of a function $f(r,\theta)$
$f_l(r)$	$\in \mathbb{C}$	circular harmonic components of a function $f(r,\theta)$
$Y(.)$	$\in \mathbb{R}^+$	Heaviside function
$P(.)$	$\in \mathbb{R}^+$	Klein-Nishina probability

Appendix B
Proof of the Convergence of (3)

We consider two measurable spaces $\mathcal{X}, \mathcal{Y} \subset \mathbb{R}^4$. Let $\mathcal{L}^2_+(\mathcal{X})$ (respectively, $\mathcal{L}^2_+(\mathcal{Y})$) be the space of square-summable functions defined on $\mathcal{X}$ (respectively, $\mathcal{Y}$) such that

$$\forall f \in \mathcal{L}^2_+(\mathcal{X}) \quad \text{and} \quad \forall X \in \mathcal{X}, \quad f(X) \geq 0.$$

Let $T : \mathcal{L}^2_+(\mathcal{X}) \longrightarrow \mathcal{L}^2_+(\mathcal{Y})$ be a positive integral operator defined by its positive integral kernel

$$(Tf)(Y) = \int_{X \in \mathcal{X}} K_T(Y,X)\, f(X)\, dX.$$

The kernel of the operator T is submitted to a positive distortion $D(Y,X) \in \mathcal{L}^2(\mathcal{X} \times \mathcal{Y})$ such that

$$\exists D_m \in \mathbb{R}^+ < \infty s.t. \quad \forall (X,Y) \in \mathcal{X} \times \mathcal{Y}, \quad D(Y,X) \leq D_m.$$

Thus, we can define a "distorted" operator $T^\Phi : \mathcal{F}_1 \longrightarrow \mathcal{F}_2$,

$$\left(T^\Phi f\right)(Y) = \frac{1}{D_m} \int_{X \in \mathcal{X}} D(Y,X)\, K_T(Y,X)\, f(X)\, dX.$$

To prove the convergence of this algorithm, we have to show that the error tends towards 0, i.e.,

$$|f^{n+1} - f^n| \underset{n \longrightarrow +\infty}{\longrightarrow} 0_{\mathcal{F}_1}.$$

This error can be written as

$$\begin{aligned} f^{n+1} - f^n &= T^{-1} \circ T^\Phi (f - f^n) \\ &= \left(Id_{\mathcal{F}_1} - T^{-1} \circ T^\Phi\right)^n \left(f^1\right). \end{aligned}$$

Providing our space with the $\mathcal{L}_2$-norm and defining the norm of the operator T as

$$|||T||| = \sup_{f\in\mathcal{F}_1} \frac{\|Tf\|_2}{\|f\|_2},$$

the convergence amounts to prove that

$$|||Id_{\mathcal{L}^2_+(\mathcal{X})} - T^{-1}\circ T^{\Phi}||| < 1.$$

Now, we can notice that $T^{-1}\circ T = Id_{\mathcal{F}_1}$ so

$$Id_{\mathcal{F}_1} - T^{-1}\circ T^{\Phi} = T^{-1}\circ\left(T - T^{\Phi}\right).$$

For $f \in \mathcal{F}_1$, we have

$$\begin{aligned}\left(T^{-1}\circ\left(T - T^{\Phi}\right)\right) f \\ = T^{-1}\left(\int_{\mathcal{X}}\left(1 - \frac{D(Y,X)}{D_m}\right) K_T(Y,X)\, f(X)\, dX\right).\end{aligned}$$

Therefore, it exists a constant M such that

$$\left(1 - \frac{D(Y,X)}{D_m}\right) \le M = 1 - \min_{(X,Y)\in\mathcal{X}\times\mathcal{Y}}\left\{\frac{D(Y,X)}{D_m}\right\} < 1.$$

In this case,

$$\begin{aligned}\left(T^{-1}\circ\left(T - T^{\Phi}\right)\right) f &\le M \times T^{-1} \\ &\quad\times\left(\int_{\mathcal{X}} K_T(Y,X)\, f(X)\, dX\right), \\ &\le M \times f\end{aligned}$$

and so

$$|||Id_{\mathcal{F}_1} - T^{-1}\circ T^{\Phi}||| \le M^2 < 1,$$

which ensures the convergence.

Now, we have to prove that the solution is the original function. At convergence, we have

$$f^{n+1} - f^n = T^{-1}\left(T^{\Phi}\left(f - f^n\right)\right) = 0.$$

The injectivity of operators implies the unicity of the solution

$$\begin{aligned}T^{-1}\left(T^{\Phi}\left(f^{n+1} - f^n\right)\right) = 0 \quad &\Longrightarrow \quad T^{\Phi}\left(f - f^n\right) = 0 \\ &\Longrightarrow \quad f^n = f.\end{aligned}$$

REFERENCES

[1] T. Beyer, D. W. Townsend, T. M. Brun, C. P. E. Kinahan, R. Roddy, J. Jerin, J. Young, L. Byars, and R. Nutt, "A combined PET/CT scanner for clinical oncology," *J. Nucl. Med.*, vol. 41, pp. 1369–1379, 2000.

[2] H. Zaidi, M. Montandon, and A. Alavi, "The clinical role of fusion imaging using PET, CT and MRI," *Magn. Reson. Imag. Clin. N. Amer.*, vol. 18, no. 1, pp. 133–149, 2010.

[3] H. Zaidi and K. F. Koral, "Scatter modelling and compensation in emission tomography," *Eur. J. Nucl. Med. Mol. Imag.*, vol. 31, pp. 761–782, 2004.

[4] P. G. Lale, "The examination of internal tissues, using gamma-ray scatter with a possible extension to megavoltage radiography," *Phys. Med. Biol.*, vol. 4, pp. 159–167, 1959.

[5] R. L. Clarke, E. N. Milne, and G. Van Dyk, "The use of Compton scattered gamma rays for tomography," *Investigate Radiol.*, vol. 11, pp. 225–235, May/Jun. 1976.

[6] G. Harding, H. Strecker, and R. Tischler, "X-ray imaging with Compton-scatter radiation," *Philips Tech. Rev.*, vol. 41, pp. 46–59, 1983.

[7] N. V. Arendtsz and E. M. A. Hussein, "Energy-spectral Compton scatter imaging—Part 1: Theory and mathematics," *IEEE Trans. Nucl. Sci.*, vol. 42, pp. 2155–2165, 1995.

[8] S. J. Norton, "Compton scattering tomography," *J. Appl. Phys.*, vol. 76, pp. 2007–2015, 1994.

[9] M. Morvidone, M. K. Nguyen, T. T. Truong, and H. Zaidi, "On the V-line Radon transform and its imaging applications," *J. Biomed. Imag. (Special Issue on Mathematical Methods for Images and Surfaces)*, 2010, doi: 10.1155/2010/208179, ID 208179, 6 pp.

[10] T. T. Truong and M. K. Nguyen, "On new v-line Radon transforms in $\mathbb{R}^2$ and their inversion," *J. Phys. A, Math. Theor.*, vol. 44, p. 075206, 2011.

[11] M. Dahlbom, D. C. Yu, S. R. Cherry, A. Chatziioannou, and E. J. Hoffman, "Methods for improving image quality in whole body PET scanning," in *Proc. Nucl. Sci. Symp. Med. Imaging Conf.*, 1991, vol. 3, pp. 1587–1591.

[12] S. Surti, R. D. Badawi, C. H. Holdsworth, G. E. Fakhri, P. E. Kinahan, and J. S. Karp, "A multi-scanner evaluation of PET image quality using phantom studies," in *Nucl. Sci. Symp. Conf. Rec.*, 2003, vol. 4, pp. 2425–2427.

[13] I. G. Zubal, C. R. Harrell, E. O. Smith, and A. L. Smith, "Two dedicated software, voxel-based, anthropomorphic (torso and head) phantoms," presented at the Int. Workshop, Nat. Radiol. Protection Board, Chilton, U.K., Jul. 1995.

[14] A. M. Cormack, "The Radon transform on a family of curves in the plane," *Proc. Amer. Math. Soc.*, vol. 83, no. 2, pp. 325–330, Oct. 1981.

[15] A. M. Cormack, "Radon's problem—Old and new," *SIAM-AMS Proc.*, vol. 14, pp. 33–39, 1984.

[16] A. Maze, J. L. Cloirec, R. Collorec, Y. Bizais, P. Briandet, and P. Bourguet, "Iterative reconstruction methods for nonuniform attenuation distribution in SPECT," *J. Nucl. Med.*, vol. 34, pp. 1204–1209, 1993.

[17] G. Rigaud, M. K. Nguyen, and A. K. Louis, "Novel numerical inversions of two circular-arc Radon transforms in Compton scattering tomography," *Inverse Problems Sci. Eng.*, 2012, doi: 10.1080/17415977.2011.653008.

[18] L. Triet, R. Chartrand, and T. J. Asaki, "A variational approach to reconstructing images corrupted by Poisson noise," *J. Math. Imag.Vis.*, 2007, doi: 10.1007/s10851-007-0652-y.

[19] H. Zaidi, "Relevance of accurate Monte Carlo modeling in nuclear medical imaging," *Med. Phys.*, vol. 26, no. 4, pp. 574–608, 1999.